Physics of Fluids

Large eddy simulation of incident flows around polygonal cylinders

Cite as: Phys. Fluids **33**, 105112 (2021); https://doi.org/10.1063/5.0063046
Submitted: 11 July 2021 • Accepted: 12 September 2021 • Published Online: 06 October 2021

Esmaeel Masoudi, Lian Gan and David Sims-Williams

Physics of Fluids ARTICLE scitation.org/journal/phf

Large eddy simulation of incident flows around polygonal cylinders

Cite as: Phys. Fluids 33, 105112 (2021); doi: 10.1063/5.0063046
Submitted: 11 July 2021 · Accepted: 12 September 2021 ·
Published Online: 6 October 2021

Esmaeel Masoudi,[a] Lian Gan,[b] and David Sims-Williams[c]

AFFILIATIONS

Department of Engineering, Durham University, Durham DH1 3LE, UK

[a]Electronic mail: esmaeel.masoudi@durham.ac.uk
[b]Author to whom correspondence should be addressed: lian.gan@durham.ac.uk
[c]Electronic mail: david.sims.williams@durham.ac.uk

ABSTRACT

In this study, we carry out large eddy simulation of incident flow around polygonal cylinders of side number $N = 5 - 8$ at Reynolds number $\mathrm{Re} = 10^4$. In total, six incidence angles (α) are studied on each cylinder ranging from face to corner orientations, thus covering the entire α spectrum. Special focus is put on the time-mean aerodynamic forces including lift, drag, and vortex shedding frequencies as well as the near wake flow features. It is found that because of y-plane asymmetry of polygonal cross sections at most incidence angles, the flow separation characteristics and hence the induced base pressure distribution and the aerodynamic forces exhibit unique and complex dependence on α and N. While the general inverse relation of drag coefficient and Strouhal number previously proposed from experimental observations at principal orientations still holds at arbitrary α, the variation of the two is found to be non-monotonic on both α and N. We also found that compared to the absolute time mean shear layer length measured from the final separation point, the extent of them stretched to the wake, measured from the cylinder center, is a powerful scaling factor for all the quantities investigated, including the wake characteristic length scales. In particular, the difference between the top and the bottom shear layer (due to geometrical asymmetry at arbitrary α) describes the variation of the non-zero time mean lift coefficient reasonably well, whose sign varies with N non-monotonically.

I. INTRODUCTION

The phenomenon of Kármán vortex shedding is a major concern in design of slender and bluff-body structures exposed to the wind and ocean current flows. Flow past a circular cylinder has been extensively studied in both experimental and numerical approaches and is one of the most canonical problems in fluid mechanics for its geometry is a fundamental element underlying many practical engineering structures.

Polygonal cylinders deviate from circular cylinders in the sense that they have geometry asymmetry at arbitrary incidence angles with an integer number N of equal length edges. Flow past polygonal cylinders partially resembles the flow around circular cylinders in terms of the formation of Kármán vortex streets[1] for Reynolds number Re $>\mathcal{O}(10^2)$. However, because of their quasi-axisymmetric shape, the local boundary layer separation behavior exhibits significant N dependent variations compared to the circular cylinder (effectively $N \to \infty$). If N is not large, flow typically separates from corners (one on the top half and the other on the bottom half) due to discontinuous change of local pressure, which is insensitive with respect to oncoming flow speed, hence Re. For small N, locally the flow behaves similarly to that over a convex corner. Even though the deflection angle and the length of the edge are both monotonic function of N, the detailed pressure gradient in the local free stream and the associated reattachment behavior renders the overall aerodynamic performance strongly non-monotonic against N. It is thus plausible that the aerodynamic forces not only vary remarkably on the principal orientations (namely, corner oriented or face oriented) as demonstrated by Xu *et al.*,[2] but also are expected to be a strongly non-linear function of their arbitrary angle of attack α with respect to the direction of the uniform oncoming flow U. Noting that corner orientation refers to a case where a corner of the polygon is on the centerline upstream and face orientation refers to a case where the middle of a face lies on the centerline upstream. As N increases to $N \geq 10$, the flow dynamics starts to approach the circular cylinder asymptotically. The number of corners becomes larger with their relative height being smaller, which could be treated as roughness elements on the surface of a circular cylinder. For instance, Cheng *et al.*[3] studied the effect of sinusoidal-shaped grooves on a circular cylinder in various Reynolds numbers in the subcritical regime.

In theses cases, Re dependence becomes important, similar to the critical Re effect on a circular cylinder.[2]

Flow around polygonal cylinders of small N, viz., square ($N=4$) and triangular ($N=3$) cylinders, has been studied extensively but rather individually. To mention a few recent works among many others about a standalone stationary cylinder, Sohankar[4] studied the wake structure of flow past a square cylinder using Smagorinsky (SMG) and dynamic-one large eddy simulation (LES) for $10^3 < \mathrm{Re} < 5 \times 10^6$, and found that global behaviors are largely Re-independent for $\mathrm{Re} > 2 \times 10^4$. They concluded that in general, the sharp-edged bodies, which tend to cause flow separation regardless of the boundary layer characteristics, are Re insensitive, especially at large Re. Hu *et al.*[5] studied flow fields and aerodynamic characteristics of rigid inclined square cylinders with yaw angles at $\mathrm{Re} = 4 \times 10^4$ using LES and found that C_D decreases with increasing yaw angle magnitude. They also found that cellular structures with lower shedding frequencies than the Kármán vortex shedding frequency are generated in the wake due to the interference of the free-end vortex pair or the base vortex pair. Yagmur *et al.*[6] studied a corner oriented equilateral triangular cylinder using particle image velocimetry (PIV) and LES. They found that increasing Re leads to a shrunk wake and backside approached stagnation points. Bai and Alam[7] studied flow around a face oriented square cylinder using two-dimensional (2D) laminar simulation and three-dimensional (3D) LES for $\mathrm{Re} \leq 10^3$ as well as PIV, hot wire, and force measurements in an open circuit wind tunnel at $10^3 < \mathrm{Re} < 4.5 \times 10^4$. They identified five flow regimes, namely, steady flow ($\mathrm{Re} < 50$), laminar flow ($50 < \mathrm{Re} < 1.6 \times 10^2$), two to three dimensional transition ($1.6 \times 10^2 < \mathrm{Re} < 2.2 \times 10^2$), shear layer transition I ($2.2 \times 10^2 < \mathrm{Re} < 10^3$), and shear layer transition II ($10^3 < \mathrm{Re}$). Jiang and Cheng[8] studied flow past a face oriented square cylinder using direct numerical simulations (DNS) for $\mathrm{Re} < 400$. They showed that the viscous drag decreases to negative values for $\mathrm{Re} \geq 154$, which is due to the increasing coverage of the backward flow on the upper and lower surfaces of the cylinder. Kumar and Tiwari[9] carried out three-dimensional numerical investigations for flow past surface mounted finite height prisms of equilateral triangle, square, and circular cross sections in laminar shear flow of $60 < \mathrm{Re} < 200$ using DNS. They found that for all the cases, St decreases with increasing shear strength for fixed Re. Moreover, with an increase in the shear intensity, drag decreases corresponding to each Re for all the tested cross sections. They also quantified the extent of nonlinear fluctuations in the wake in terms of "degree of stationarity" and showed that it confirms that multiple frequencies are responsible for the wake nonlinearity at $150 < Re < 200$ for the triangular cross section alone. Jiang[10] studied wake transition for flow past a square cylinder in corner orientation (as called diamond-shaped cylinder) using DNS at $\mathrm{Re} \leq 300$. They found that the wake becomes three-dimensional at $\mathrm{Re}_{cr} \approx 121$ with a swap in vortex shedding mode accompanied by the disappearance of global vortex dislocation which changes monotonically with increasing Re.

Studies of cylinders with $N > 4$ are sparse. Tian and Li[11] studied a polygonal cylinder of $N=24$ in a low-speed wind tunnel to find a low drag solution for their prototype supporting frames. They found a much lower critical Reynolds number and 40% lower drag with a low level fluctuation compared to a circular cylinder under similar flow conditions. Tian and Wu[12] investigated inviscid flow and low-Reynolds number ($\mathrm{Re} < 200$) viscous flow around 2D polygonal cylinders at corner orientation for even values of N. Using conformal mapping, they showed that for the inviscid flow, the global pressure difference along the surface is inversely proportional to a sufficiently large value of N. For the viscous flow, however, they derived the relation between the first critical Re and N, and found that this Re monotonically decreases as N increases for both unsteady and steady flows. Khaledi and Andersson[13] studied flow past hexagonal ($N=6$) cylinders in face and corner orientations using DNS at $\mathrm{Re} = 100, 500, 1000$. They concluded that St is slightly higher in face orientation. They also explained that the Kármán vortices roll up closer to the body in the case of a face orientation and thus result in a shorter formation region and a higher St. Recalling the wake characteristics of a face and corner oriented square cylinders, they suggested that the wake of a face oriented and corner oriented hexagons resembles the square cylinder of the same orientation, respectively, and therefore the after body plays a minor role.

In a recent wind tunnel experiment, Xu *et al.*[2] for the first time systematically studied the aerodynamic characteristics of polygonal cylinders for $2 \leq N \leq 16$ over $10^4 \leq Re \leq 10^5$ using a combination of force measurement, smoke flow visualization, and planar PIV. They showed that given polygons of $N \leq 8$, the flow eventually separates (could reattach and separate again) at so-called maximum width points, which is insensitive to the Re range tested and as a result, no appreciable change is observed on the drag coefficient C_D and St. They also showed that similar to circular cylinders, at the two principal orientations, the St and C_D values are inversely related. Later, Wang *et al.*[14] showed that the mechanism of vortex formation from the polygon surface is correlated with some length scales, describing the near field wake. These scaling factors include the length of the reversed flow zone L_r^*, the recirculation bubble width D_b^*, the vortex formation length L_f^*, and the characteristic wake width D_w^*. The empirical relations between these scaling factors and various kinematic and dynamic quantities suggest that the understanding of the polygonal cylinder wake could be unified to that of the circular cylinder wake. That is, the shape and the orientation information of the polygons could be made irrelevant as long as appropriate longitudinal and transverse length scales are used to scale the quantities in question.

In a continuing wind tunnel PIV experiment, Wang *et al.*[1] presenting detailed data of the wake of the polygonal cylinders $3 \leq N \leq 16$ with face and corner orientation at $\mathrm{Re} = 1.6 \times 10^4$ studied the dependence on N and the cylinder orientation of the mean velocity, the Reynolds stresses, and the coherent vortex structures in the near wake. They showed that the circulation of individual shed vortex grows to its maximum value at the vortex formation length (L_f^*) and then decays downstream due to the combined effect of viscosity and vortex cancelation. They also found that cases of $N=8$ at corner orientation and $N=5$ at face orientation show the smallest L_f^*, D_w^* and the lowest Reynolds stress magnitude, with the smallest velocity deficit and fastest velocity recovery in the near wake. On the other hand, cases of $N=6$ at corner orientation and $N=4$ at face orientation are found to have the largest vortex strength and adverse pressure gradient in the reverse flow zone, which results in the smallest velocity recovery rate in the near wake.

In this study, we focus on polygonal cylinders of $N = 5, 6, 7, 8$ using three-dimensional LES to investigate the effect on the aerodynamic forces and near wake flow subjected to the complete range of angle of attack α with respect to U. The simulations were performed at

$\mathrm{Re} = 10^4$, which is within the range tested experimentally by Xu *et al.*[2] This experimental work suggests that flow does not undergo transition for $N \leq 8$ cylinders, at least for $\mathrm{Re} \lesssim 10^6$ (no transition is likely to occur at even higher Re). Therefore, our result should be valid for a wide Re regime. Furthermore, according to the measurements at their principal orientations, extreme aerodynamic forces and strong nonlinearity were observed on $N \leq 8$ polygons. Polygons of larger N tend to have less extreme responses and behave asymptotically to circular cylinders.

In this manuscript, we will also focus on the time-mean aerodynamic quantities and their correlations with the characteristic length scales extracted from the mean velocity field.

II. COMPUTATIONAL MODELING AND NUMERICAL SETUP

A. Computational domain and boundary conditions

The computational domain is sketched in Fig. 1. R_c and R_i denote the circum-circle and in-circle radius, and the corresponding diameters are D_c and D_i, from which Re defined by different diameters are denoted as Re_c and Re_i, respectively. In this study, constant $\mathrm{Re}_i = 10^4$ based on D_i is utilized, which is α independent. The cylinder axis is aligned with z-axis, and the incoming free stream flow velocity U is set at the desired α with respect to the x'-axis. A body-fitted O-type structured grid is applied to ensure grid orthogonality, which is commonly used for flow around cylinder problems.[15–23] In $x' - y'$ plane, the grids are hexahedral shaped. The $x-y$ plane is aligned with incoming flow direction (U). The number of cells in the radial and circumferential directions is denoted as N_r and N_θ. The grid size grows exponentially in the radial direction (r) from the body surface and is uniformly spaced in the circumferential direction (θ) and the spanwise direction (z). The growth rate in the r direction is set such that the maximum y^+ is below unity; $y^+ = yu_\tau/\nu$ with $u_\tau = \sqrt{\tau_0/\rho}$, where τ_0 is the wall shear stress. Following previous 3D LES studies at various Re,[17,22–28] a spanwise length $L_z = \pi D_c$ with $N_z \approx 48 \times D_c/D_i$ cells and periodic boundary conditions at both ends are used to minimize the unrealistic topology associated with the application of the periodic boundary conditions, prevent periodic artifacts, and achieve satisfactory accuracy of aerodynamic forces and the wake flow patterns. The inlet/outlet surfaces are indicated in Fig. 1. At the inflow surface, uniform free stream flow velocity U resolved into x' and y' directions is imposed. At the outflow surface, a Neumann boundary condition is imposed to avoid the flow reflection. No-slip condition is applied at cylinder surface. The domain outer boundary is set at $20\times$ cylinder diameters ($20D_i$) from cylinder center.

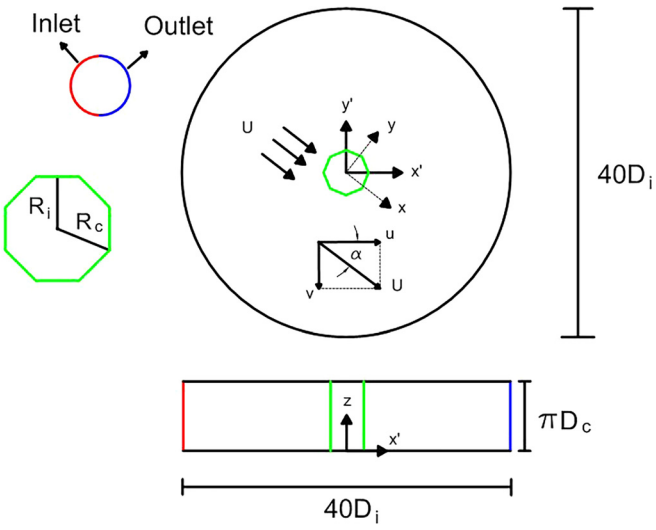

FIG. 1. Computational domain and problem configuration for polygonal cylinders in body fitted O-type structured grids. Not to scale.

B. The LES solver

The governing equation for the current 3D constant SMG LES simulations, with kernel $G = G(x, \Delta)$ and Δ being the grid filter width, is

$$\frac{\partial \bar{u}_i}{\partial x_i} = 0, \tag{1}$$

$$\frac{\partial \bar{u}_i}{\partial t} + \frac{\partial \bar{u}_i \bar{u}_j}{\partial x_j} = -\frac{1}{\rho}\frac{\partial \bar{p}}{\partial x_i} + \frac{\partial}{\partial x_j}\left[\nu\left(\frac{\partial \bar{u}_i}{\partial x_j} + \frac{\partial \bar{u}_j}{\partial x_i}\right) + \tau_{ij}\right], \tag{2}$$

where ν is the kinematic viscosity, and $\bar{u}$ and $\bar{p}$ are the filtered velocity and filtered pressure, respectively. In the spatially filtered Navier–Stokes equations, the stress term $\tau_{ij} = \overline{u_i u_j} - \bar{u}_i \bar{u}_j$ is modeled using the eddy-viscosity type SGS model of Smagorinsky,[29] which is based on Boussineq's assumption,

$$\tau_{ij} - \frac{2}{3}k_t \delta_{ij} = -2\nu_t\left(\bar{S}_{ij} - \frac{1}{3}\bar{S}_{kk}\delta_{ij}\right), \tag{3}$$

$$\bar{S}_{ij} = \frac{1}{2}\left(\frac{\partial \bar{u}_i}{\partial x_j} + \frac{\partial \bar{u}_j}{\partial x_i}\right), \tag{4}$$

where $\bar{S}_{ij}$ is the rate of strain tensor computed from the resolved scales and ν_t and k_t are SGS viscosity and turbulent kinetic energy, respectively; see Fureby *et al.*[30] for a comprehensive review of all SGS models.

In the algebraic SMG model,[29] ν_t and k_t are calculated explicitly under the assumption of local equilibrium balance between production and dissipation of k_t. The Smagorinsky coefficient $C_s = 0.1$ is adopted based on several validated studies of flow around circular cylinders,[16,17,19–21] and a near-wall damping formulation suggested by Van Driest[31] is implemented,[18,19,21]

$$\Delta = \min\left(\frac{k_v}{C_\Delta}, \Delta\right) y\left[1 - \exp\left(\frac{-y^+}{25}\right)\right], \tag{5}$$

where the Von Kármán constant $k_v = 0.4187$ and model constant $C_\Delta = 0.158$. No wall function is used.

In this study, OpenFOAM is used to perform LES simulations. The second order scheme, backward, is used for time integration. The predictor-corrector PISO (Pressure-Implicit with Splitting of Operators) is used to decouple and iteratively solve the pressure and velocity fields. The pressure is solved by a geometric agglomerated algebraic multi-grid (GAMG) solver. Three PISO corrector are used for each time step to minimize uncertainty of the final results. A dynamic time step is utilized to keep the maximum Courant number unity.

TABLE I. Grid configuration and sensitivity study for a hexagonal cylinder in face orientation.

Case	L_z/D_c	N_r	N_θ	N_z	$y^+_{\max}$	$\overline{C_D}$	St
Coarse	π	120	120	56	1.3	1.469	0.193
Medium	π	168	168	56	1.08	1.686	0.187
Fine	π	216	216	56	0.88	1.647	0.187
Very fine	π	264	264	56	0.75	1.628	0.187

C. Validation

A grid sensitivity study was performed for a hexagonal cylinder ($N=6$) in face orientation, and the results are summarized in Table I, with the maximum y^+, time-mean drag coefficient $\overline{C_D}$, and Strouhal number St. The drag coefficient and the lift coefficient are defined in the conventional way as

$$C_D = \frac{F_D}{\frac{1}{2}\rho U^2 (L_z D_x)}, \tag{6}$$

$$C_L = \frac{F_L}{\frac{1}{2}\rho U^2 (L_z D_x)}, \tag{7}$$

where F_D and F_L are, respectively, the total drag and lift forces. ρ is the density of the working fluid; $L_z D_x$ is the projected area in the streamwise direction with D_x being the projected width of the cylinder, which is a function of α.

The time-averaged aerodynamic forces are calculated over an appropriate interval of $t^* = tU/D_i$, after the transient time period when the flow becomes quasi-steady. This time interval is equivalent to a minimum of 30 vortex shedding cycles. St is defined as

$$\mathrm{St} = \frac{f_{vs} D_x}{U}, \tag{8}$$

where the vortex shedding frequency f_{vs} is determined from the C_L spectrum. A distinctive and unique peak is identifiable in the spectrum of all the cases, confirming the classical Kármán vortex shedding in the wake.

Table II lists the results of $\overline{C_D}$ and St compared with the experimentally measured quantities in Xu *et al.*[2] for face and corner oriented cylinders at similar Re. Note that Re in Xu *et al.*[2] is defined based on D_x, which is slightly different from Re_i. The small difference between D_i, D_c, and D_x decreases for larger N and for some polygons and orientations. In general, the simulation results are comparable to experimental results with reasonable accuracy. Analysis also shows that the adopted "Fine" mesh in Table II resolves more than 90% of the turbulent kinetic energy (k_t) (except near the separation points, in which it is roughly 80%), and therefore the current LES is considered well resolved.[32]

TABLE II. $\overline{C_D}$ and St compared to experimental results in Xu *et al.*[2] "F" and "C" stand for face and corner orientation, respectively. N_θ varies slightly for different N to ensure equal number of meshes on each surface.

	Present		Xu *et al.*[2]	
	$\mathrm{Re}_i = 1.0 \times 10^4$		$\mathrm{Re} = 1 \times 10^4$	
Case	$\overline{C_D}$	St	$\overline{C_D}$	St
5F	0.96	0.245	1.146	0.202
5C	2.25	0.152	1.627	0.140
6F	1.65	0.187	1.375	0.178
6C	2.11	0.145	1.866	0.138
7F	1.66	0.172	1.663	0.155
7C	1.48	0.162	1.228	0.169
8F	1.84	0.159	1.566	0.148
8C	1.34	0.199	0.95	0.195

III. RESULTS AND DISCUSSION

A. Force coefficients and Strouhal number

In order to study the effect of incidence angle α on flow characteristics, 6 equal-spaced αs are studied for each cylinder between the corner and the face orientations, which effectively cover all possible orientations. Note that the absolute step size $\Delta\alpha$ varies for different polygons. We define the incidence angle $\alpha^* = \alpha/\alpha_T$, where $\alpha_T = 180^\circ/N$. In this respect, $\alpha^* = 0$ corresponds to corner orientation and $\alpha^* = 1$ face orientation, and cylinder rotates clockwisely in between; $\Delta\alpha^*$ is thus fixed at 0.2. For easier comparison, Strouhal number and force coefficients are redefined using D_i to be St_i and $\overline{C_{D_i}}$, instead of using D_x, which is α dependent. The maximum discrepancy ΔD_x occurs for the $N=5$ cylinder at $\alpha^* = 0, 1$, which is $1.176D_i$, and is smaller for larger N, e.g., $\Delta D_x = 1.082D_i$ for $N=8$ at $\alpha^* = 0$.

Figures 2(a) and 2(b) show the dependence of α^* on $\overline{C_{D_i}}$ and St_i. As it can be seen, orientation has a strong effect on the two quantities. For $N=5$, St_i and $\overline{C_{D_i}}$ behave monotonically with increasing α^*, and the change is more substantial over $\alpha^* \geq 0.6$. For other polygons, the change is not monotonic, i.e., they display maximum/minimum values not at the principal orientations. For $N=6$, St_i starts to increase from $\alpha^* = 0.4$ and reaches the largest value at $\alpha^* = 0.8$. $\overline{C_{D_i}}$ shows a similar but opposite behavior, which experiences a drop in $0.4 \leq \alpha^* \leq 0.6$. $N=7$ and $N=8$ cylinders display large variation at small α^*, which is in contrast to the other two cylinders. The $\overline{C_{D_i}}$ behaviors are very similar, but the St_i displays appreciable differences for $\alpha^* \leq 0.6$. The general behavior of $\overline{C_{D_i}}$ and St_i agrees with the findings of most cylinder shaped bodies. We will return to this point later. It is plausible that higher vortex shedding frequency f_{vs} corresponds to less stable shear layer which results in shed vorticies with smaller circulation and therefore lower $\overline{C_{D_i}}$. It is confirmed by the pressure distribution to be discussed later.

Figures 2(c) and 2(d) present the variation of separation angles from both the upper surface θ_s^U and the lower surface θ_s^L, as α increases. Zero separation angle $\theta_s = 0^\circ$ is defined as a vector from the cylinder center pointing to the—U direction and θ_s is defined as the angle between $\theta_s = 0^\circ$ and the vector from the cylinder center to the boundary separation point. θ_s is determined from examining the time mean velocity field and the associated streamlines, and they are marked geometrically in Fig. 3. Both the primary separation point (PSP) and the secondary separation point (SSP) are marked in Figs. 2(c), 2(d), and 3, and they always occur at corners. The PSP is the

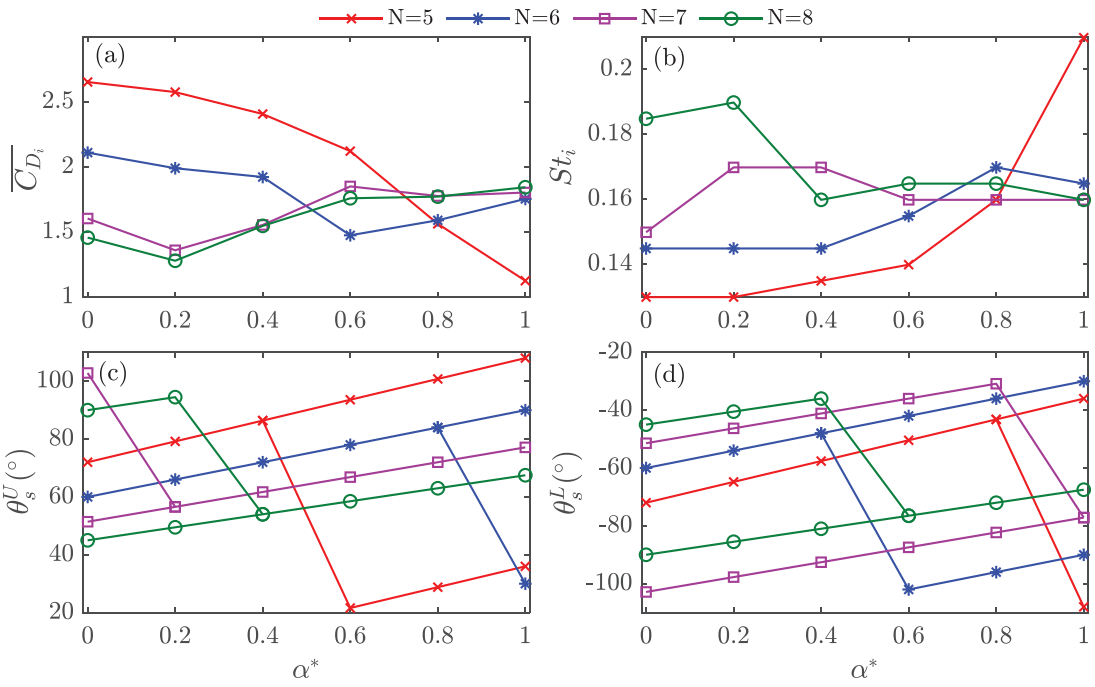

FIG. 2. Dependence of $\overline{C_{D_i}}$ (a) and St_i (b) and the separation angle θ_s on α^*. Superscript *U* and *L* on θ_s stand for the upper (c) and lower surfaces (d), respectively. In (c) and (d), both the primary separation angle and the secondary separation angle are indicated.

corner at which the boundary layer separates for the first time, and the SSP is the corner at which the flow separates eventually. Whenever SSP appears, it always locates at the downstream corner on the same edge as PSP. Boundary layer separation is confirmed from the time-resolved shear layer (instantaneous vorticity) behavior, as well as the mean vorticity field (opposite signed vorticity layer attach to the surface). The latter will be discussed in Sec. III C. In Figs. 2(c) and 2(d), for each N, there are two values of θ_s at a given α^* over a range depending on N. Between the two θ_s, PSP is always the one with smaller magnitude $|\theta_s|$. Note that SSP is different from boundary layer re-attachment point, which usually locates on an edge downstream of PSP and is highly oscillatory, in agreement with the flow visualization[2] at the present Re. Boundary layer re-attachment behavior is not the focus of this work and will be discussed in a separate paper.

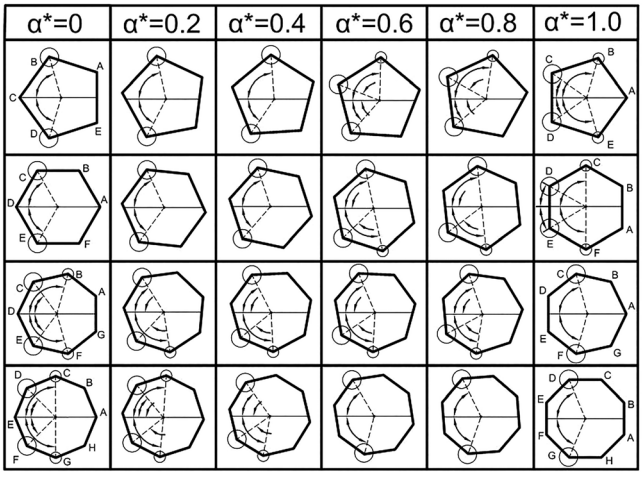

FIG. 3. Separation point at different α^*. The primary separation points (PSP) are labeled with big circles and the secondary separation points (SSP) with small circles. Free stream flow comes from the left.

Examination of Figs. 2(c), 2(d), and 3 reveals some separation phenomena which perhaps are not so obvious. The separation mechanism can be categorized into two groups, viz., $N=5$, 6 and $N=7$, 8. As expected, there is at least one PSP on each of the upper and lower surface. As α^* increases from zero, SSP starts to appear on $N=5$, 6, which then end with both PSP and SSP symmetrically at $\alpha=1$. In contrast, $N=7$, 8 start with both PSP and SSP, and end with PSP only. In other words, the total number of separation points PSP+SSP is an increasing function of α^* for $N=5$, 6, and a decreasing function for $N=7$, 8. PSP+SSP varies between 2 and 4 for all cases, which suggests that there are two unique critical α^* s for each N at which the separation behavior changes appreciably. The critical α^* seems to be a necessary condition for discontinuous changes of $\overline{C_{D_i}}$ and St_i.

Comparing PSP+SSP to the overall trend of $\overline{C_{D_i}}$ and St_i in Figs. 2(a) and 2(b) also suggests that increasing the total number of separation points results in an overall decrease in $\overline{C_{D_i}}$ and an overall increase in St_i. It is plausible that the number of separation points is directly associated with the stability of the boundary layer and therefore has a significant impact on the wake. Roughly speaking, appearance of SSP means that re-attachment occurs between PSP and SSP. The instability in the re-attachment region results in higher frequency unsteadiness and then in lower drag. This instability is reflected in a dynamic

flapping behavior of the detached shear layer and is reflected by higher St_i. The shear layer flapping also leads to transient attachment to and detachment from SSP in some cases.

While there is always a single PSP on each of the upper and the lower surface, because of their quasi-axisymmetric geometry, the distribution of SSP is unbalanced. For instance, the only SSP is on the upper surface on $N=5$ cylinder but is on the lower surface on $N=6$ cylinder for $\alpha^* < 1$. This discrepancy is related to the mean lift direction, which will be discussed later. As N is larger, both the deflection angle between successive edges and the edge length become smaller, and the separation and reattachment behavior gets very subtle and sensitive to α. For instance, for the case $N=8$ at $\alpha^* = 0.4$, the time-averaged separation bubble appears to be very thin on the lower surface upstream of the labeled PSP.

At the present Re, pressure is the dominant contributor of the aerodynamic force over skin friction. It then makes sense to investigate the pressure distribution variation over the α spectrum. Figure 4 illustrates the time mean pressure coefficient defined as

$$\overline{C_p} = \frac{\bar{p} - p_\infty}{\frac{1}{2}\rho U^2}, \tag{9}$$

where $\bar{p}$ the time mean pressure and p_∞ is the constant free stream pressure. Here we also take the spanwise averaged $\bar{p}$. In all the simulated cases, no spanwise variation can be observed for all the time mean quantities presented in this article.

For illustration purpose, in Fig. 4 the cylinders are fixed in position while the incoming flow angle is set at different α. In this way, the positions of the corners are fixed. Here, the polar angle θ is used to describe the coordinates of the cylinder surface, where $\theta = 0^\circ$ is along the horizontal direction pointing to the right, as marked. The range of θ is chosen to be $-180^\circ \le \theta \le 180^\circ$, where positive and negative θ directions are also marked, together with the tested incidence angles α^*. The corners are labeled and also marked on the θ axis. It should be noted that the range of windward/leeward surfaces changes with respect to the incidence angles. Windward surface is defined from the top SSP (or PSP if SSP does not exist), through the windward stagnation point, to the SSP on the bottom surface. For instance, in $N=5$, windward surface is B–C–D for $\alpha^* = 0$ and B–C–D–E for $\alpha^* = 1$.

A distinct characteristic of $\overline{C_p}$ distribution is its abrupt change of value at corners where separation event occurs. The extent of $\overline{C_p}$ change is labeled as ΔC_P in Fig. 4(a). For instance, corner D is always a separation point on $N=5$ and $N=8$ cylinders and corner C for $N=6$ and $N=7$. PSP typically exhibits the most abrupt and the strongest ΔC_P, while those at SSP is weaker, similar to that at the corner closest to the base point near the leeward surface stagnation point - corner A in most cases. ΔC_P at other corners in the separated region is typically insignificant, barely visible in some corners on $N \ge 6$, leading to relatively constant pressure distribution along the edges inside this region (the range of small $|\theta|$ in all the cases). This is similar to the C_P distribution at the back surface over a circular cylinder. It reassures the more important dynamic role played by PSP than SSP. In this respect, the relative ΔC_P magnitude is a characterization of the nature of a corner and reflects the transition of separation point as α^* changes, for instance, the transition of PSP from B to C at $\alpha^* = 0.4$ (to $\alpha^* = 0.6$) on $N=5$. Another example is the disappearance of SSP at B from $\alpha^* = 0$ to 0.2 on $N=7$.

The drag coefficient $\overline{C_{D_i}}$ has intrinsic relation with $\overline{C_p}$, especially over the leeward surface inside the separated region (the small $|\theta|$ range), as the distribution $\overline{C_p}$ over the windward surface in the vicinity

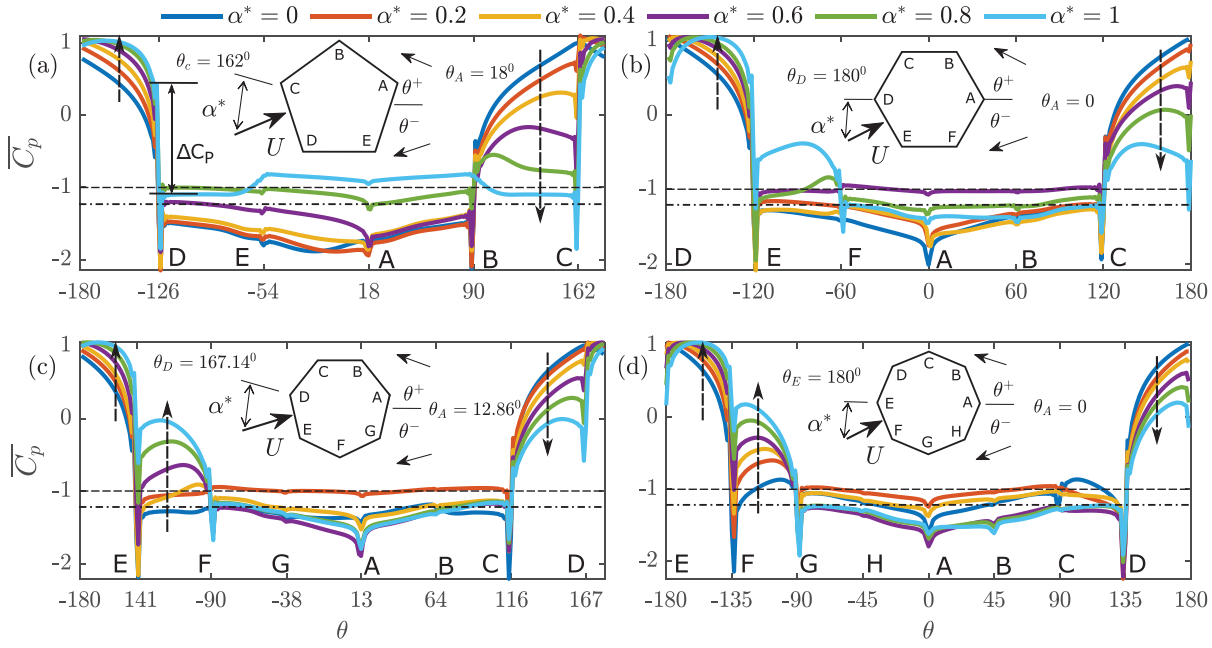

FIG. 4. Dependence of the spanwise averaged mean pressure coefficient $\overline{C_p}$ distribution on α^*. ——: reference value $\overline{C_p} = -1$; — · —: base pressure coefficient for circular cylinder at similar Re (subcritical),[33] $C_p \approx -1.2$. In (a), ΔC_p represents the degree of pressure change at corners of separation. The vertical dashed line arrows indicate the general monotonic variation of $\overline{C_P}$ in the direction of increasing α^*. The surfaces without dashed line arrows marked do not entirely follow a monotonic variation of $\overline{C_P}$.

of the windward stagnation point is fairly universal. The distribution of $\overline{C_p}$ over the leeward surface has strong dependence on both N and α^*.

The dependence on N is mainly reflected by the minimum pressure $\overline{C_{p\,\min}}$, which occurs at corner A. Among the N case studied, $N=5$ cylinders shows the lowest $\overline{C_{p\,\min}} \approx -2$, which is significantly lower than the value on a circular cylinder measured at similar Re experimentally,[33] which is $\overline{C_{p\,\min}} \approx -1.2$. As N increases, this value increases accordingly, but all < -1.2. On $N=5$ cylinder, $\overline{C_{p\,\min}}$ occurs at $\alpha^* = 0.2$, which equals the value in between corner E and A at $\alpha^* = 0$. On $N=6$, 7, 8 cylinders, $\overline{C_{p\,\min}}$ occurs at $\alpha^* = 0, 0.6, 0.6$, respectively, all at corner A. Comparing to the maximum $\overline{C_{D_i}}$ values in each N presented in Fig. 2(a), the α^* values match. Considering the maximum pressure coefficient $\overline{C_{p\,\max}}$ over the leeward surface, it can be observed that this value decreases from $N=5$ [Fig. 4(a), over EB] to $N=8$ [Fig. 4(d), over GC]. Therefore, the difference $(\overline{C_{p\,\max}} - \overline{C_{p\,\min}})$ decreases monotonically as N increases. It is then reasonable to deduce that as N further increases, and $N \to \infty$, $\overline{C_{p\,\max}}$ and $\overline{C_{p\,\min}}$ would collapse on to the line $\overline{C_p} \approx -1.2$, i.e., asymptotically to the circular cylinder case.

Dependence of $\overline{C_p}$ on α^* is more complex. Perhaps expected, $\overline{C_p}$ on the main windward surface (viz. surface CD, DE, DE, EF, on $N = 5 - 8$, respectively) is an increasing function of α^* in all cases as they gradually become perpendicular to U. However, the magnitude change is mild. Larger change of $\overline{C_p}$ magnitude occurs on the surface next to this windward surface on the upper part of the cylinder but is a monotonically decreasing function of α^*. On $N=7$, 8 cylinders, an additional surface displays significant dependence of $\overline{C_p}$ on α^*, viz., surface EF and FG. These two surfaces are next to the windward surface on the lower part of the cylinder. The other surfaces without dashed line arrows marked do not follow a monotonic trend strictly. Over these surfaces, $\overline{C_p}$ variation is relatively small, and they are mostly the back surfaces. Those back surfaces hence all the surfaces on the $N=5$ cylinder are monotonic in terms of $\overline{C_p}$ distribution or marginally so, which explains the behavior of $\overline{C_{D_i}}$. On the other cylinders, the $\overline{C_p}$ distribution is non-monotonic, which makes it tricky to relate to their $\overline{C_{D_i}}$ behavior. Nevertheless, if we sort $\overline{C_{p\,\min}}$ (at A) or the average $\overline{C_p}$ over these back surfaces for a given N in ascending order, and $\overline{C_{D_i}}$ in descending order, the corresponding α^* approximately matches. It thus suggests that the (fairly constant) pressure distribution on the back surface has an important impact on the drag. The exact relation to $\overline{C_{D_i}}$ is of course an integration effect of the $\overline{C_p}$ distribution on all the surfaces. Pressure drag obeys a strong linear relationship to the total drag $\overline{C_{D_i}}$ for each cylinder at various incident angles (figure not shown). It typically contributes to $\gtrsim 96\%$ of $\overline{C_{D_i}}$.

It is not difficult to deduce that because their quasi-axisymmetric geometry, $\overline{C_p}$, distribution at intermediate α^*, i.e., at non principal orientations, will result in non-zero mean lift coefficient $\overline{C_L}$. This is shown in Fig. 5. The lift coefficient is also redefined here as $\overline{C_{Li}} = \overline{C_L} \times D_x/D_i$. The distribution of D_x based lift coefficients is very similar, therefore not shown. The magnitude of $\overline{C_{Li}}$ is about 10% of $\overline{C_{Di}}$, but it shows an interesting behavior, which perhaps is not predictable immediately. That is, $N=5$ and $N=8$ show a positive lift, whilst $N=6$ and $N=7$ show a negative lift, even through the tested α range is positive, in the sense that they all start from the corner orientation and step to the face orientation clockwisely. It also means that if we keep rotating the cylinders beyond the face orientation, $\overline{C_{Li}}$ will become opposite signed; hence, the "overall" aerodynamic response is

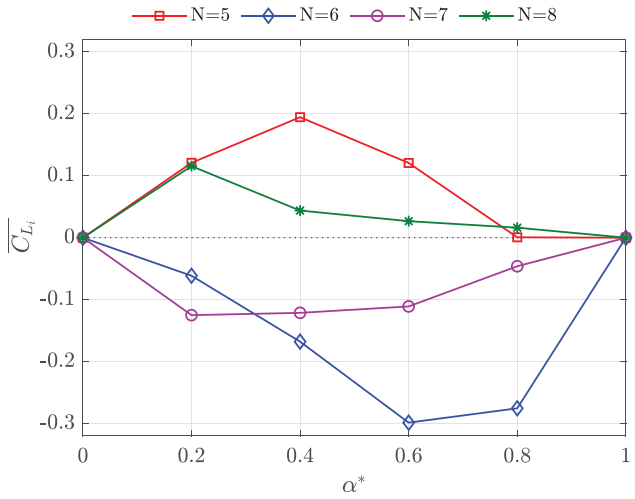

FIG. 5. Dependence of the time mean lift coefficient $\overline{C_{Li}}$ on α^*.

converged. The direction of $\overline{C_{Li}}$ and α^* at which the maximum magnitude occurs can be inferred more clearly by the mean shear layer behavior, which we will discuss in Sec. III C. For $N=6$, 7, 8 the maximum lift magnitude occurs when $\overline{C_{D_i}}$ is minimum. For $N=5$ however, since the minimum drag occurs at $\alpha^* = 1$, which is a symmetric condition, lift is approximately zero and the maximum lift occurs at $\alpha^* = 0.4$.

B. Near wake asymmetry

Since $\overline{C_p}$ distribution over the back surfaces is likely to have an important impact on the aerodynamic forces as discussed above, it makes sense to have further investigation of the near field wake in terms of their time mean characteristics. Figure 6(a) demonstrates the asymmetric distribution of the time mean streamwise velocity $\bar{U}$ about the $x-$ axis. The contour pattern, as well as the location of the stagnation point, qualitatively reflects the degree of asymmetry. To quantify the asymmetry, we examine the $\bar{U}$ distribution along the y direction going through the point where the strongest reversed flow occurs and between the two points of the local maximum velocity $\bar{U}_{\max}$. The two end points of the line (x_{mx1}, y_{mx1}) and (x_{mx2}, y_{mx2}) are just outside the two mean shear layers, which will be discussed later. The $\bar{U}$ distribution of all the cases studied is presented in Fig. 6(b), which displays the classical bell shape if being offset by $\bar{U}_{\max}$ and is reasonably symmetric about $y=0$. However, closer inspection does reveal non-trivial asymmetry near the location of $\bar{U}_{\max}$ (the tail region) and inside the recirculation bubble (the top region).

The extent of the near wake skew-symmetry is quantified and presented in Fig. 7. In (a), the asymmetry of y_{mx1} and y_{mx2} to the wake centerline $y=0$ is calculated. Recall that they characterize the lateral distance to the outer edge of the shear layer at $x=x_r$. As such, they are also proportional to the recirculation bubble width. The sign of $(y_{mx1} + y_{mx2})$ indicates the skew direction. If $(y_{mx1} + y_{mx2}) > 0$, the upper half of the bubble is fatter; otherwise, it is thinner. As the cylinders rotate unidirectionally from the same corner orientation, $N=5$ shows a fatter lower bubble for all α^*, whilst $N=6$, 7 show a fatter bubble on the upper part. This is consistent with the $\overline{C_L}$ variation

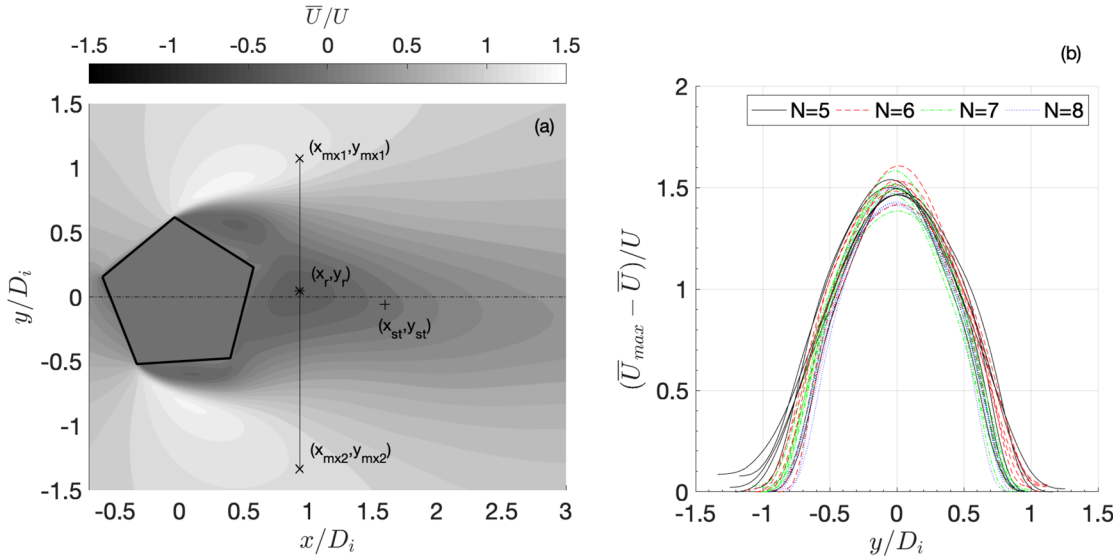

FIG. 6. (a) $\bar{U}$ in the near wake behind $N=5$ cylinder at $\alpha^* = 0.2$. Point (x_r, y_r), marked by $*$ is where maximum reversed velocity, i.e., minimum $\bar{U}$, occurs; point (x_{st}, y_{st}), marked by $+$ is the stagnation point; points (x_{mx1}, y_{mx1}) and (x_{mx2}, y_{mx2}), marked by $\times$, are maximum $\bar{U}$ denoted by $\bar{U}_{max}$ occurring along the y direction going through (x_r, y_r). (b) Distribution of $(\bar{U}_{max} - \bar{U})$ along the line between (x_{mx1}, y_{mx1}) and (x_{mx2}, y_{mx2}) for all the 24 cases studied.

shown in Fig. 5 and the asymmetric number of separation points PSP+SSP shown in Fig. 3. On $N=8$ cylinder, the fatter side switches at $\alpha^* = 0.4$, but the difference is fairly small, which is also in line with the small $\overline{C_L}$ magnitude and the symmetric PSP+SSP.

A better quantification for the degree of asymmetry of $\bar{U}_{\max}$ distribution about $y=0$, as that shown in Fig. 6, is by calculating μ, defined as

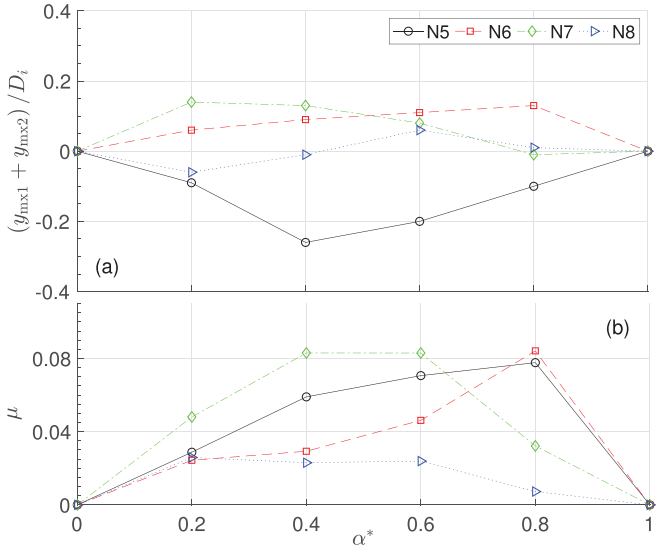

FIG. 7. Near wake asymmetry quantification. (a) Asymmetry of y_{mx1} and y_{mx2} to the wake centerline, $(y_{mx1} - |y_{mx2}|)$; y_{mx2} is negative. (b) Degree of $(\bar{U}_{max} - \bar{U})$ asymmetry about $y=0$, as shown in Fig. 6(b), quantified by μ.

$$\mu^2 = \frac{\int [\psi(y) - \psi(-y)]^2 dy}{\int [\psi(y) + \psi(-y)]^2 dy}, \tag{10}$$

where $\psi(y) = \bar{U}_{max} - \bar{U} \geq 0$ at $x = x_r$ and is a function of y. μ calculates the ratio of the skew-symmetric part of ψ to the symmetric part of it. It takes into account the effect of offset y_r about $y=0$. Dependence of μ on α^* is presented in Fig. 7(b). It is clear that all α^* between the two principal orientations display non-trivial asymmetry about $y-$ axis. However, first μ does not generally follow a decreasing trend as N as the degree of axisymmetry increases. $N=7$ shows larger μ values than $N=6$, which is off-trend in this sense. Second, μ itself is skewed toward face orientation for $N=5$, 6, e.g., $\psi(y)$ is mostly skew-symmetric at $\alpha^* = 0.8$, more than doubled than $\alpha^* = 0.2$ in terms of the μ value. μ is more symmetric about α^* for $N=7$ and 8 cylinders. $N=8$ has the weakest μ, as well as the weakest y_{mx} asymmetry, as expected. The extent of skew-symmetry continues increasing for $x > x_r$, up to $x \sim 10D_i$, beyond which the spatial resolution becomes low.

Figure 8(a) shows the location of x_r at which $\psi(y)$; hence, μ is measured. x_r characterizes the recirculation bubble length x_{st} as $x_r \sim (1/2)x_{st}$, where (x_{st}, y_{st}) denotes the coordinates of the wake stagnation point [see Fig. 6(a)]. It is obvious that x_r increases monotonically with α^* for $N=5$, but for $N=6$, 7 abrupt increment of x_r occurs at intermediate α^*, where the value is approximately 50% higher than that at other α^*, whose $x_r \approx D_i$ and is fairly constant. Figure 8(b) shows the correlation of x_r with the value of $\bar{U}$ at point (x_r, y_r), which is the maximum reversed flow inside the recirculation bubble. It is shown to be well correlated negatively with x_r, which suggests that the longer the recirculation bubble, the stronger is the reversed velocity intensity. The correlation can be reasonably described by

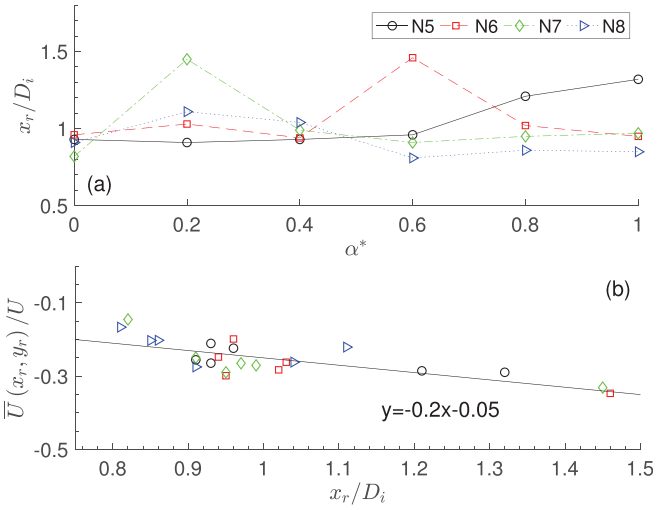

FIG. 8. (a) The streamwise location x_r of the maximum reversed velocity and (b) its correlation with the reversed velocity value denoted as $\bar{U}(x_r, y_r)$.

$$\frac{\bar{U}(x_r, y_r)}{U} \approx -0.2\left(\frac{x_r}{D_i}\right) - 0.05. \tag{11}$$

No clear monotonic dependence of $\bar{U}(x_r, y_r)$ on N is observed.

C. Separated shear layers

The asymmetry of aerodynamic forces and the recirculation bubble can be better explained by examining the separated shear layers, represented by the time mean spanwise vorticity $\omega = \omega_z D/U$, which is shown in Fig. 9. It is not difficult to observe that the shear layers exhibit clear difference in terms of their length and thickness, which depend on both N and α^*. Here we focus on their length only. Shear layer thickness and intensity are more correlated with the instantaneous shear layer flapping motion. For instance, the thickest shear layer typically occurs for cases having only PSP where the flapping motion is strong. For $N = 5 - 8$, the longest shear layer occurs at $\alpha^* = 1, 0.6, 0.2$, and 0.2, respectively, which agree well with the largest x_r presented in Fig. 8(a). The variation of the length on α^* is also in line with St_i and $\overline{C_{D_i}}$ (inversely) shown in Fig. 2. Secondary thin shear layers attached to the surface of the cylinder can also be observed in all the cases. They are associated with the boundary layer separation and reattachment, which are of the opposite sign of the separated main shear layers in the outer region.

Another distinguishing feature is the asymmetry of the shear layer length on top and bottom surfaces, originated from the asymmetric positions of the separation points; see Fig. 3. Quantification of the shear layer length is presented in Fig. 10. We define length $\bar{L}_\omega$ from the cylinder center to the x coordinate of the end point subject to a threshold of $\omega = 3$. The threshold value is insensitive to the trend of the results hence the conclusion. The shear layer curvature, which is fairly small, is not taken into account. $\bar{L}_\omega$ is essentially the x coordinate of the shear layer ending point. Also shown is $\bar{L}_\omega$ measured from the final separation point, viz., SSP, or PSP if SSP does not exist; see Fig. 3. It is denoted as $\bar{L}_\omega^{SP}$, which characterizes the absolute length of the shear layer. The maximum $\bar{L}_\omega^{SP} \approx 1.8D_i$, which occurs on the bottom of $N = 5$ and the top of $N = 7$. On $N = 6, 8$, maximum $\bar{L}_\omega^{SP}$ reduces to $1.5D_i$.

Comparing the two quantities, it can be noticed that even when $\bar{L}_\omega^{SP}$ differs on the upper and the lower surfaces clearly, the shear layers terminate at similar x locations, i.e., the distance between the two solid lines, $\Delta\bar{L}_\omega$, is small at the same α^*. As N increases, $\Delta\bar{L}_\omega$ decreases as expected, since for a circular cylinder $N \to \infty$, it should reduce to zero. $N = 5$ cases display different trends. At small α^*, the shear layer lengths $\bar{L}_\omega^{SP}$ are similar, but $\bar{L}_\omega$ are different according to the

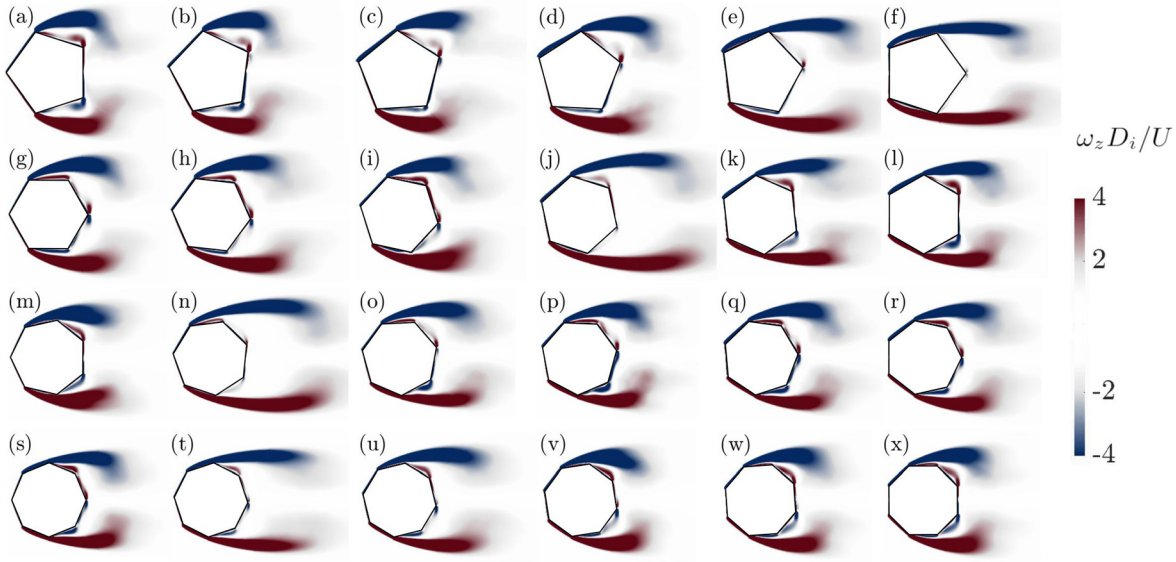

FIG. 9. Time mean spanwise vorticity $\omega_z D_i/U$ of different polygonal cylinders. Row number increases with N (a–f: $N = 5$, g–l: $N = 6$, n–r: $N = 7$, s–x: $N = 8$); column number increases with α^*.

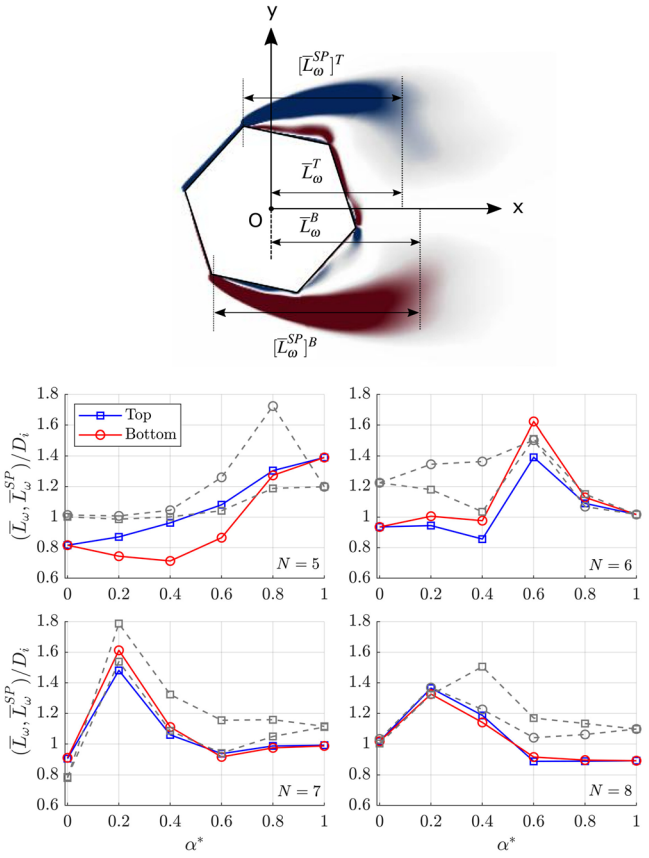

FIG. 10. Definition of shear layer length and their spanwise averaged time mean values; $\bar{L}_\omega$ on solid lines, and that measured from the final separation point, $\bar{L}_\omega^{SP}$ on dashed lines.

separation point locations. The relative magnitude of the two quantities also indicates the position of the final separation point relative to the cylinder center. In most cases, $\bar{L}_\omega^{SP} \gtrsim \bar{L}_\omega$, meaning that the final separation point is on the windward half of the cylinder.

Figure 10 also shows some interesting observations of $\bar{L}_\omega$ in addition to the clear asymmetric pattern. $N = 5$ cylinders demonstrate clear increasing $\bar{L}_\omega$ on α^* monotonically (if the average value of top and bottom is taken), whilst the other cylinders have clear maximum $\bar{L}_\omega$ at an intermediate α^*. This behavior matches that of x_r shown in Fig. 8(a) as well as $\overline{C_{Di}}$ and St_i in Fig. 2. For a given N, α^* at which the maximum $\Delta\bar{L}_\omega$ occurs matches that for the maximum $\overline{C_L}$ shown in Fig. 5. It therefore suggests that $\bar{L}_\omega$ could be a better scaling factor for the shear layer strength than the absolute shear layer length $\bar{L}_\omega^{SP}$ when considering the asymmetry effect. For the same cylinder, the maximum $\bar{L}_\omega$ change is about $0.7D_i$ (on the bottom surface) for $N = 5 - 7$ and $0.5D_i$ for $N = 8$.

Note that since $\bar{L}_\omega^{SP}$ and $\bar{L}_\omega$ are time mean quantities, they take into account the oscillation motion of the vortex shedding in the streamwise distance hence the instantaneous shear layer length. This effect is clearly observable in instantaneous vortex shedding pattern in a cycle, as presented in Fig. 11 for selected cases. Here the minimum $\overline{C_{Di}}$ (also the maximum St_i) in each N is chosen. All of these cases demonstrate delayed vortex shedding leading to large $\bar{L}_\omega$ compared to the same N at other α^*. In these demonstrated cases, the shear layers are stretched further to the wake with the upper and lower shear layers interacting less strongly compared to other cases. Having less mutual interaction helps with shear layer stability and delays vortex shedding. Oscillation of the streamwise vortex shedding location can be observed clearly in $N = 5$ case (a–d) for instance and shear layer flapping motion can be seen in $N = 7$ case (i–l), more obvious toward the downstream portion of the shear layers.

In addition to the streamwise oscillation, the presented cases all have SSP on their surface (see Fig. 3). Furthermore, as mentioned earlier in Sec. III A, shear layer flapping motion can result in temporary disappearance of SSP as shear layer detaches from that corner. This effect typically only occurs in the present cases in Fig. 11. Examples are $N = 6$, 7 both on surface EF; $N = 6$ on surface BC and DE; and $N = 8$ on surface CD. The other case which is not presented here is $N = 7$ and $\alpha^* = 0$ on surface BC and EF (see Fig. 3). For other cases, whenever boundary layer reattaches after PSP, it stays attached and separates again at SSP without temporary detachment of shear layer as a result of the flapping motion. The reattachment process fluctuates in terms of the reattachment position between PSP and SSP.

D. Scaling parameters

Previous sections revealed some underlying connections in those time mean quantities. In this section, we test their correlations by combining all the cases studied. It has been established previously that $\overline{C_D}$ and St are well correlated with wake formation length L_f and wake width D_w, respectively, for polygonal cylinders at principal orientations.[14] Figure 12 illustrates that these scaling laws still reasonably apply for arbitrary α^*. Here we take L_f as the x coordinate of the point at which the maximum turbulence kinetic energy occurs, which is well defined. The asymmetric effect is neglected as the offset y coordinate of the point is very small. D_w is taken to be the wake displacement width at L_f. For direct comparison, $\overline{C_D}$ and St here are based on the projection length D_x. The $\overline{C_D}$ scaling follows the empirical linear relation proposed by Wang *et al.*[14] well, whilst St has slightly higher values in the present numerical study but also follows a second-order polynomial function shape. Note that according to Wang *et al.*,[14] Strouhal number plotted in (b) is based on D_w and is denoted as St^+.

Figure 13(a) displays the dependence of $\overline{C_{D_i}}$ and St_i on $\bar{L}_\omega$, which is the extent of the time mean shear layer in the x direction. Here $\bar{L}_\omega$ is the average value of the two shear layers [see Fig. 10], viz., $\bar{L}_\omega = (\bar{L}_\omega^T + \bar{L}_\omega^B)/2$, the superscript standing for the top and the bottom side, respectively. Evidently, both quantities scale with $\bar{L}_\omega$ reasonably well by arbitrary functions. St_i behaves like a quadratic function similarly as Fig. 12(b). $\overline{C_{D_i}}$ is apparently a decreasing function of $\bar{L}_\omega$ and approaches asymptotically to a value ≈ 1.3. Inferred by the fundamental relation of $\overline{C_{D_i}}$ and the base pressure, the variation of the averaged base pressure coefficient $\overline{C_p}$ is also presented. $\overline{C_p}$ here is calculated as the area averaged value between the last separation points on the top and the bottom surfaces (see Figs. 3 and 4). As can be speculated, the base pressure and $\overline{C_{D_i}}$ are well correlated negatively (figure not shown) with the former converging asymptotically to −1 for large $\bar{L}_\omega$. This means that the further the shear layer extends to the downstream distance, the higher the base pressure and therefore the lower the drag since the pressure over the windward surfaces does not depend strongly on N and α^* as reflected by Fig. 4. It then seems to

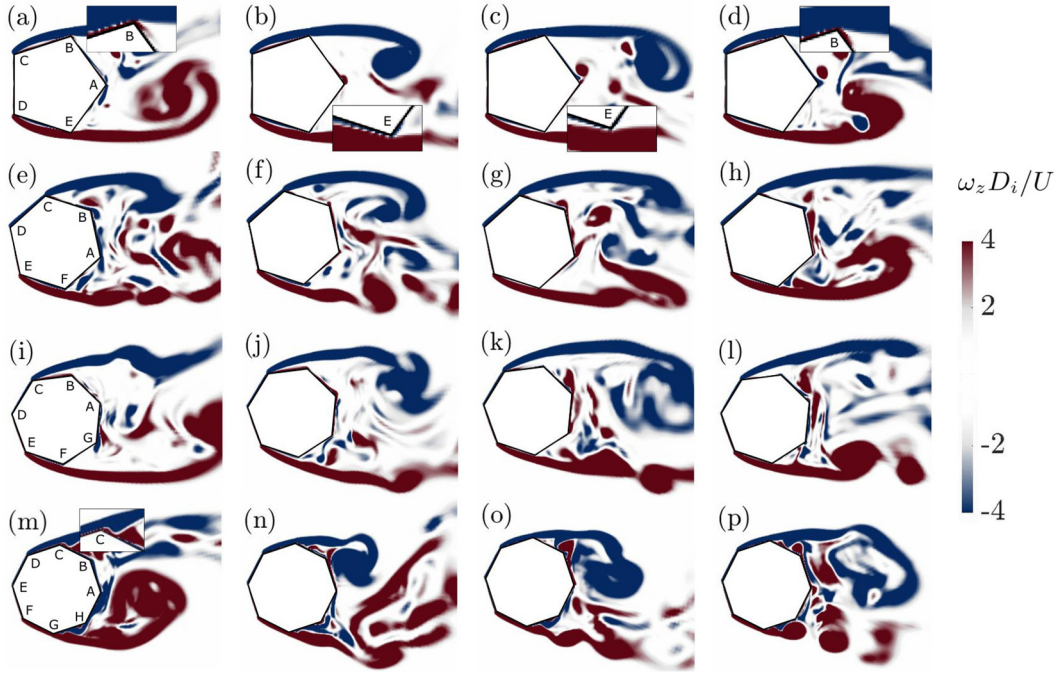

FIG. 11. Instantaneous spanwise vorticity fields at mid span for selected cases. From the first column (a,e,i,m) to the last (d,h,l,p), the phase angle $\varphi = 0$ ($C_L = 0$), $\pi/2$, π, and $3\pi/2$, respectively. The first row to the last are for $(N = 5, \alpha^* = 1)$, $(N = 6, \alpha^* = 0.6)$, $(N = 7, \alpha = 0.2)$ and $(N = 8, \alpha^* = 0.2)$, respectively.

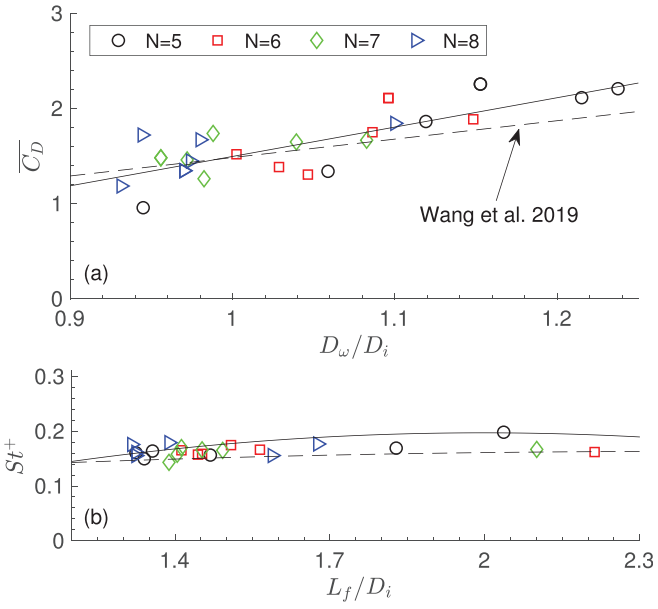

FIG. 12. The correlation between $\overline{C_D}$ and St (based on the projection width D_x) with the wake width D_w and the formation length L_f. The results of Wang *et al.*[14] are for $\mathrm{Re} = 1.6 \sim 5.1 \times 10^4$ and at principal orientations only. Polynomial fittings are applied, first order in (a) and second order in (b).

suggest that the shear layer intensity (circulation per unit length) is not a dominant factor here. Comparing Figs. 8 and 10, it can be speculated that $\bar{L}_\omega \sim x_r$ (figure not shown, data collapse well), and therefore $\bar{L}_\omega$ is also expected to be a proper scaling factor for the maximum reversed flow velocity $\bar{U}(x_r, y_r)$. This is shown in Fig. 13(b). With Eq. (11), the relation between $\bar{L}_\omega$ and x_r can be approximated by

$$\frac{\bar{L}_\omega}{D_i} \approx 1.4\frac{x_r}{D_i} - 0.36. \tag{12}$$

Figures 12 and 13(a) suggest that the three characteristic length scales are also well correlated. This is confirmed in Fig. 13(c). L_f (as well as x_r as mentioned above) increases with $\bar{L}_\omega$, and the two are approximately linearly dependent for $\bar{L}_\omega > D_i$. D_w, the characteristic wake width (the length scale in the y direction), is shown to be a much weaker function of N and α^* than the length scales in the x direction. The ratio of the maximum and the minimum values is only ≈1.3. It varies as a decreasing function of $\bar{L}_\omega$ and converges to D_i slowly. It is worth mentioning that D_w based on the momentum width does not scale with $\overline{C_D}$ well as the pressure distribution along the y direction at $x = L_f$ is a significant factor.

While the average of the top and the bottom shear layers scales with $\overline{C_{D_i}}$, it is found that the difference of the two, viz., $(\bar{L}_\omega^T - \bar{L}_\omega^B)$, seems to be related to $\overline{C_{Li}}$ (as well as $\overline{C_L}$ because of its similar behavior, not shown), as inferred by Figs. 5 and 10, and shown in Fig. 14. It demonstrates that not only the sign of $\overline{C_{Li}}$ and $(\bar{L}_\omega^T - \bar{L}_\omega^B)$ is consistent

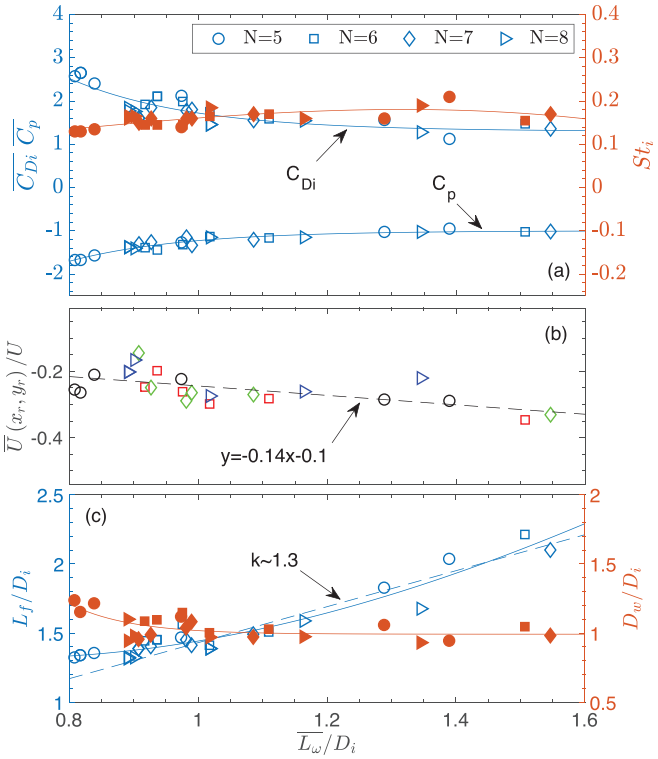

FIG. 13. (a) Correlation between $\overline{C_D}$, St_i and the averaged base pressure with the averaged $\bar{L}_\omega$; (b) correlation between $\bar{L}_\omega$ and the maximum reversed flow velocity $\bar{U}(x_r, y_r)$; (c) correlations of the length scales L_f, D_w, and $\bar{L}_\omega$. The solid lines are arbitrary fitting functions; the dashed lines in (b) and (c) are linear fitting functions. The linear fitting in (c) is for $\bar{L}_\omega/D_i \geq 1$.

($N = 5$, 8 positive and $N = 6$, 7 negative), but also the variation of the two variables. The solid line represents

$$\frac{\bar{L}_\omega^T - \bar{L}_\omega^B}{D_i} = \overline{C_{Li}}, \tag{13}$$

as the two variables vanish together because of symmetry. Although this line is not the best linear fit of the data, it describes the data

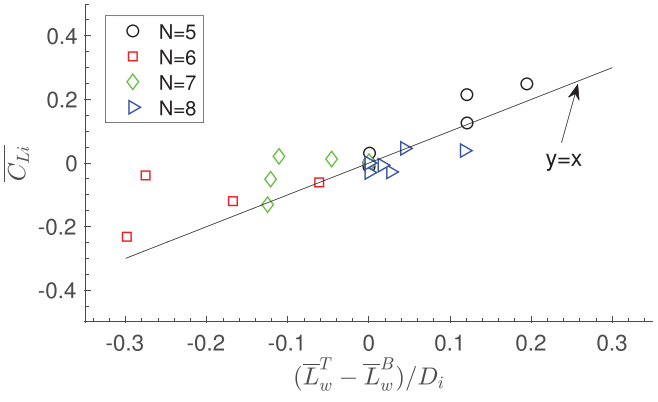

FIG. 14. Correlation between $\overline{C_{Li}}$ and the difference of $\overline{L_\omega}$ between the top and the bottom shear layers.

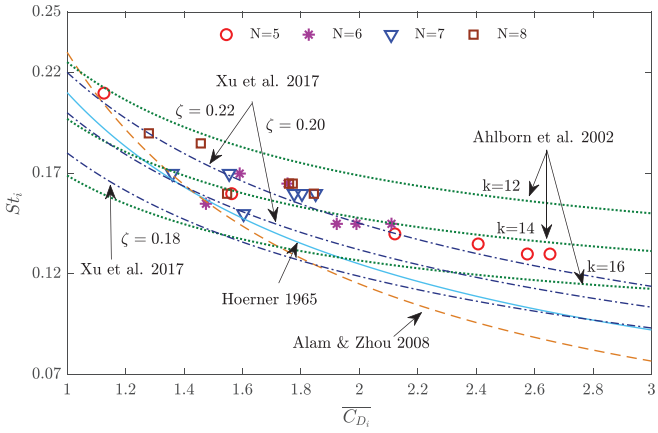

FIG. 15. The correlation between $\overline{C_{D_i}}$ and St_i compared to the empirical relations proposed by Hoerner,[34] Ahlborn, Seto, and Noack,[35] Alam and Zhou,[36] and Xu *et al.*[2]

distribution reasonably well. In contrast, the asymmetry of the absolute shear layer length $\bar{L}_\omega^{SP}$ does not display a clear trend with $\overline{C_{Li}}$ (figure not shown, but it can be inferred by inspecting Fig. 10); the sign is not consistent at least. This seems to be a puzzling result since $\overline{C_L} \sim \Gamma = \int \omega \, ds$, where Γ is the circulation around the cylinder, s being the area element. The integration can be performed over a control volume containing the cylinder and the near wake, outside which (the time mean) ω is negligible, and therefore both shear layers are included completely. The reason for $(\bar{L}_\omega^T - \bar{L}_\omega^B)$ being the better scaling factor than the $\bar{L}_\omega^{SP}$ difference perhaps is that the former somehow takes into account the shear layer intensity as well as the attached boundary layer and its separated region, which might merely be a coincidence.

Finally, the inverse relation between the drag coefficient and Strouhal number has been well acknowledged following equations proposed by Hoerner,[34] Ahlborn *et al.*,[35] Alam and Zhou,[36] and Xu *et al.*[2] as

$$0.21 = C_D^{0.75} St, \tag{14}$$

$$k = 2^{11/2}\pi \frac{C_D St}{C_D + 1}, \tag{15}$$

$$0.23 = C_D St, \tag{16}$$

$$\zeta = C_D^{0.6} St, \tag{17}$$

where k is an energy parameter which varies in general with different bluff body shapes and ζ is an empirical constant, and Eq. (17) was proposed for polygonal cylinders at principal orientations in particular. Figure 15 reassures that these formulas work for incident flow angles when the universal length scale D_i is used to define the two variables. Among the formulas, Eqs. (15) ($k \approx 14$) and 17 ($0.20 \lesssim \zeta \lesssim 0.22$) seem to fit the data better. The best fit ζ value agrees with the experimental findings[2] well, albeit slightly different definitions are used.

IV. CONCLUSION

In this paper, incident flow around polygonal cylinders of side number $N = 5, 6, 7, 8$ is numerically studied using LES at $\mathrm{Re} = 10^4$. In total, six dimensionless angles of attack α^* are tested, which covers

the entire spectrum. A constant SMG model is adopted, and the simulation results are validated against the available experimental measurements. This work only focuses on the time mean aerodynamic and wake flow quantities. Their quasi-axisymmetric and discretized geometry leads to the following observations.

Flow separates primarily at corners. In some cases, it reattaches and then separates for the second time at secondary separation points, which are also corners. However, in these cases, shear layers may temporarily detach from the secondary separation points because of the shear layer flapping motion. This happens in the 4 asymmetric cases displayed in Fig. 11 plus one symmetric case of $N = 7, \alpha^* = 0$. In the 4 asymmetric cases, the shear layers tend to be stretched further into the wake and delay vortex shedding, compared to other cases.

The location of the separation points is asymmetric about the x axis, depending heavily on N and α^*. This results in complex surface pressure distribution leading to complex time mean aerodynamic responses and wake asymmetry. In particular, drag coefficient and Strouhal number vary non-monotonically with α^*. The non-zero lift coefficient and the wake symmetry are non-monotonic functions of N. Their apparently random behaviors are correlated with the features of the time mean shear layers.

By combining all the cases, we found that the extent of the time mean shear layer stretched into the wake ($\overline{L_w}$), instead of the absolute length of the shear layer, seems to be a proper parameter which scales with the aerodynamic forces. It scales well with the base pressure of the cylinders and hence drag coefficient and Strouhal number, as well as the maximum reversed flow velocity in the recirculation bubble. $\overline{L_w}$ also scales with the formation length, the wake width, and the location, where the maximum reversed flow occurs. If $\overline{L_w}$ difference between the top and the bottom shear layers is considered, it scales with the mean lift coefficient. Finally, drag coefficient and Strouhal number for incident polygonal cylinders also follow the established inverse relation well. The detailed instantaneous dynamics of the separated shear layers associated with the fundamental vortex shedding mechanism will be elaborated in a separate manuscript.

ACKNOWLEDGMENTS

The authors would like to thank the Advanced Research Computing center of Durham University and the Royal Society International Exchanges (IECNSFC201061) for their support. This study was funded by Durham University doctoral scholarship (DDS) programme.

DATA AVAILABILITY

The data that support the findings of this study are available from the corresponding author upon reasonable request.

REFERENCES

[1]Q. Wang, L. Gan, S. Xu, and Y. Zhou, "Vortex evolution in the near wake behind polygonal cylinders," Exp. Therm. Fluid Sci. **110**, 109940 (2020).
[2]S. Xu, W. Zhang, L. Gan, M. Li, and Y. Zhou, "Experimental study of flow around polygonal cylinders," J. Fluid Mech. **812**, 251–278 (2017).
[3]W. Cheng, D. Pullin, and R. Samtaney, "Large-eddy simulation of flow over a grooved cylinder up to transcritical reynolds numbers," J. Fluid Mech. **835**, 327–362 (2018).
[4]A. Sohankar, "Flow over a bluff body from moderate to high reynolds numbers using large eddy simulation," Comput. Fluids **35**, 1154–1168 (2006).
[5]G. Hu, K. Tse, K. Kwok, and Y. Zhang, "Large eddy simulation of flow around an inclined finite square cylinder," J. Wind Eng. Ind. Aerodyn. **146**, 172–184 (2015).
[6]S. Yagmur, S. Dogan, M. H. Aksoy, I. Goktepeli, and M. Ozgoren, "Comparison of flow characteristics around an equilateral triangular cylinder via piv and large eddy simulation methods," Flow Meas. Instrum. **55**, 23–36 (2017).
[7]H. Bai and M. M. Alam, "Dependence of square cylinder wake on reynolds number," Phys. Fluids **30**, 015102 (2018).
[8]H. Jiang and L. Cheng, "Hydrodynamic characteristics of flow past a square cylinder at moderate reynolds numbers," Phys. Fluids **30**, 104107 (2018).
[9]P. Kumar and S. Tiwari, "Effect of incoming shear on unsteady wake in flow past surface mounted polygonal prism," Phys. Fluids **31**, 113607 (2019).
[10]H. Jiang, "Three-dimensional wake transition of a diamond-shaped cylinder," J. Fluid Mech. **918**, A35 (2021).
[11]X. Tian and S. Li, "Scientific measurements of disturbance on the prototype stands in a low speed wind tunnel," Exp. Res. Aerodyn. **25**(3), 1–6 (2007) (in Chinese).
[12]z. W. Tian and Z. N. Wu, "A study of two-dimensional flow past regular polygons via conformal mapping," J. Fluid Mech. **628**, 121–154 (2009).
[13]H. A. Khaledi and H. I. Andersson, "On vortex shedding from a hexagonal cylinder," Phys. Lett. A **375**, 4007–4021 (2011).
[14]Q.-Y. Wang, S.-J. Xu, L. Gan, W.-G. Zhang, and Y. Zhou, "Scaling of the time-mean characteristics in the polygonal cylinder near-wake," Exp. Fluids **60**, 181 (2019).
[15]X.-Y. Lu and C. Dalton, "Calculation of the timing of vortex formation from an oscillating cylinder," J. Fluids Struct. **10**, 527–541 (1996).
[16]M. Breuer, "Numerical and modeling influences on large eddy simulations for the flow past a circular cylinder," Int. J. Heat Fluid Flow **19**, 512–521 (1998).
[17]M. Breuer, "A challenging test case for large eddy simulation: High Reynolds number circular cylinder flow," Int. J. Heat Fluid Flow **21**, 648–654 (2000).
[18]S. Atluri, V. Rao, and C. Dalton, "A numerical investigation of the near-wake structure in the variable frequency forced oscillation of a circular cylinder," J. Fluids Struct. **25**, 229–244 (2009).
[19]M. Breuer, G. De Nayer, M. Münsch, T. Gallinger, and R. Wüchner, "Fluid–structure interaction using a partitioned semi-implicit predictor–corrector coupling scheme for the application of large-eddy simulation," J. Fluids Struct. **29**, 107–130 (2012).
[20]S. Kim, P. A. Wilson, and Z.-M. Chen, "Numerical simulation of force and wake mode of an oscillating cylinder," J. Fluids Struct. **44**, 216–225 (2014).
[21]S. Kim, P. A. Wilson, and Z.-M. Chen, "Effect of turbulence modelling on 3-D LES of transitional flow behind a circular cylinder," Ocean Eng. **100**, 19–25 (2015).
[22]R. Wang, S. Cheng, and D. S. Ting, "Effect of yaw angle on flow structure and cross-flow force around a circular cylinder," Phys. Fluids **31**, 014107 (2019).
[23]R. Wang, S. Cheng, and D. S.-K. Ting, "Numerical study of roundness effect on flow around a circular cylinder," Phys. Fluids **32**, 044106 (2020).
[24]A. Travin, M. Shur, M. Strelets, and P. Spalart, "Detached-eddy simulations past a circular cylinder," Flow Turbul. Combust. **63**, 293–313 (2000).
[25]A. G. Kravchenko and P. Moin, "Numerical studies of flow over a circular cylinder at Re$D = 3900$," Phys. Fluids **12**, 403–417 (2000).
[26]D. Labbé and P. Wilson, "A numerical investigation of the effects of the spanwise length on the 3-D wake of a circular cylinder," J. Fluids Struct. **23**, 1168–1188 (2007).
[27]S. Wornom, H. Ouvrard, M. V. Salvetti, B. Koobus, and A. Dervieux, "Variational multiscale large-eddy simulations of the flow past a circular cylinder: Reynolds number effects," Comput. Fluids **47**, 44–50 (2011).
[28]K. Zhang, H. Katsuchi, D. Zhou, H. Yamada, and Z. Han, "Numerical study on the effect of shape modification to the flow around circular cylinders," J. Wind Eng. Ind. Aerodyn. **152**, 23–40 (2016).
[29]J. Smagorinsky, "General circulation experiments with the primitive equations: I. the basic experiment," Mon. Weather Rev. **91**, 99–164 (1963).
[30]C. Fureby, G. Tabor, H. Weller, and A. Gosman, "A comparative study of subgrid scale models in homogeneous isotropic turbulence," Phys. Fluids **9**, 1416–1429 (1997).
[31]E. R. Van Driest, "On turbulent flow near a wall," J. Aeronaut. Sci. **23**, 1007–1011 (1956).

[32]S. B. Pope, "Ten questions concerning the large-eddy simulation of turbulent flows," New J. Phys. **6**, 35 (2004).
[33]C. H. Williamson, "Vortex dynamics in the cylinder wake," Annu. Rev. Fluid Mech. **28**, 477–539 (1996).
[34]S. F. Hoerner, "Fluid-dynamic drag, practical information on aerodynamic drag and hydrodynamic resistance," *Fluid-Dynamic Drag* (1965), pp. 0–2, 2–8, available at http://ftp.demec.ufpr.br/disciplinas/TM240/Marchi/Bibliografia/Hoerner.pdf.
[35]B. Ahlborn, M. L. Seto, and B. R. Noack, "On drag, strouhal number and vortex-street structure," Fluid Dyn. Res. **30**, 379 (2002).
[36]M. M. Alam and Y. Zhou, "Alternative drag coefficient in the wake of an isolated bluff body," Phys. Rev. E **78**, 036320 (2008).